Error analysis of a practical energy density sensor

John W. Parkins
RTH Systems, 135 Storm Road, Groton, New York 13073

Scott D. Sommerfeldt
Department of Physics, Brigham Young University, N241 ESC, Provo, Utah 84602

Jiri Tichy
Acoustics Department, The Pennsylvania State University, Applied Science Building, North Atherton Street, State College, Pennsylvania 16802

(Received 22 July 1999; revised 13 March 2000; accepted 15 March 2000)

The investigation of an active control system based on acoustic energy density has led to the analysis and development of an inexpensive three-axes energy density sensor. The energy density sensor comprises six electret microphones mounted on the surface of a 0.025-m (1 in.) radius sphere. The bias errors for the potential, kinetic, and total energy density as well as the magnitude of intensity of a spherical sensor are compared to a sensor comprising six microphones suspended in space. Analytical, computer-modeled, and experimental data are presented for both sensor configurations in the case of traveling and standing wave fields, for an arbitrary incidence angle. It is shown that the energy density measurement is the most nearly accurate measurement of the four for the conditions presented. Experimentally, it is found that the spherical energy density sensor is within ±1.75 dB compared to reference measurements in the 110–400 Hz frequency range in a reverberant enclosure. The diffraction effects from the hard sphere enable the sensor to be made more compact by a factor of $\frac{2}{3}$ compared to the sensor with suspended microphones. © *2000 Acoustical Society of America.* [S0001-4966(00)04906-7]

PACS numbers: 43.58.Fm, 43.50.Ki [SLE]

INTRODUCTION

Research in active noise control (ANC) systems has led scientists to investigate the performance of various cost functions such as structural intensity,[1] wave number amplitude,[2] volume velocity,[3] and, most commonly, potential energy density.[4] (The cost function of an ANC system is the function that is minimized as a result of the ANC algorithm.) Sommerfeldt and Nashif, in 1992, proposed using the sum of the acoustic energy densities at discrete points in space as a cost function for controlling acoustic fields in ducts.[5] Nashif constructed a single-axis energy density sensor using instrumentation microphones, and conducted ANC experiments in ducts with promising results.[6] This research led to the development of an ANC system for use in three-dimensional acoustic fields using the total energy density as a cost function.[7–9] In the course of this work on controlling three-dimensional acoustic fields, it was necessary to develop and characterize the performance of a three-axes energy density sensor.

Multiple sensors were needed for the ANC system, which was targeted for use in commercial applications such as aircraft cabins. Therefore, high-precision instrumentation microphones were prohibitively expensive for use in the sensor. Electret microphones manufactured by Lectret Corp. (model 1270A) costing $15 each were chosen for the sensor microphones. Calibration was also an issue since the use of digital calibration filters for each microphone in the sensor was computationally expensive for a controller. Therefore, it was necessary to understand the effects of microphones mismatched in sensitivity and phase, consistent with inexpensive electret microphones, on the calculation of the acoustic quantities in question. The sensors would be used in reverberant fields, therefore the performance of a sensor in a standing wave field was of particular interest.

Since the error analysis of the total energy density measurement requires investigating the errors in the particle velocity and pressure estimates, the errors in potential and kinetic energy density as well as intensity require little additional work, and are useful for gaining insights into the total energy density measurement. All four measurements are functions of the acoustic pressure and/or particle velocity. In this paper, the measurement errors in potential, kinetic, and total energy density as well as intensity are investigated for two sensor configurations. One configuration has the microphones suspended at points in space (referred to as a two-point sensor), while the other has microphones mounted on the surface of a hard sphere (referred to as a spherical sensor).

It is convenient to first study the bias errors (or offset errors) of a single-axis sensor which can be analyzed in greater detail due to its relative simplicity. The bias error equations for a single-axis sensor are investigated, while those of a three-axes sensor are beyond the scope of this work. The understanding gained from the study of the single-axis sensor yields insights into the error mechanisms in a three-axes sensor. Ultimately, the measurement errors of a three-axes energy density sensor are determined for some special cases through computer simulation and experimental measurement.

The bias errors of the spherical sensor are determined for the case of a one-dimensional standing wave field with arbitrary reflection coefficient and incident angle, when the measurement microphones have a sensitivity and phase mismatch. The bias errors in potential energy density, kinetic energy density, total energy density, and intensity are reported and compared to those of the two-point sensor. Analysis of the two-point sensor yields insights into the performance of the spherical sensor. It will be shown that an inexpensive yet robust spherical energy density sensor can be fabricated with sufficient accuracy for use in practical active control systems.

I. BACKGROUND

A sensor that is capable of measuring the total acoustic energy density is a vector-field sensor, since the particle velocity vector must be determined. Typically, vector-field probes, such as intensity sensors, comprise two small microphones separated by a known distance. The acoustic pressure and velocity are estimated by using finite sum and finite difference approximations, respectively. The measurement errors associated with the two-point sensor have been studied at length, especially as they relate to the intensity measurement.[10] Much less effort has been dedicated to understanding the errors of a total energy density measurement.

Early work concerning the measurement of the total energy density of an airborne acoustic field was conducted by Wolff and Massa in 1933.[11] Using three pressure gradient microphones and a single pressure microphone, the three orthogonal vector components of the particle velocity and the pressure at a point in space were measured. From these four measured quantities, the total energy density was calculated. Wolff and Massa determined, through experimentation, that the squared pressure field in an enclosure had greater spatial variation compared to the total energy density field. Wolff and Massa found that ''Practically, the use of three pressure gradient microphones with their axes mutually perpendicular plus a pressure microphone obtains the effect of averaging the readings of four pressure microphones placed at random distances from each other and several wave-lengths apart....''[11] In other words, Wolff and Massa's energy density sensor had the advantage of using a single localized instrument comprising four sensors to achieve the same results as four randomly distributed sensors. Wolff and Massa's research indicates that a control system based on a total energy density measurement would be less sensitive to placement of the error sensor than one based on the squared pressure.

Cook and Schade, in 1974, investigated a configuration for an energy density sensor and its use for measurements in a reverberant chamber.[12] They investigated the spatial variances of one-, two-, and three-dimensional potential and total energy density fields. The variance of the total energy density field in a reverberant enclosure was estimated to be one-half that of the squared pressure field. Cook and Schade constructed a three-dimensional energy density sensor using three pairs of microphones. The performance limitations of the energy density sensor were not disclosed.

Elko, in 1991, investigated the diffraction effects of a spherical probe on intensity, potential energy density, and kinetic energy density measurements.[13] Elko investigated a single-axis vector-field sensor consisting of two microphones embedded on the surface of a hard sphere. Elko demonstrated that diffraction from the hard sphere causes beneficial biases which offset systematic biases for the finite sum and finite difference approximations in the pressure and velocity measurements, respectively, for most incidence angles. Elko derived these results for perfectly matched microphones, with regard to sensitivity and phase, in a traveling plane wave field with variable angles of incidence. No investigation was made into the accuracy of a total energy density measurement, or how the sensor would perform in a standing wave field.

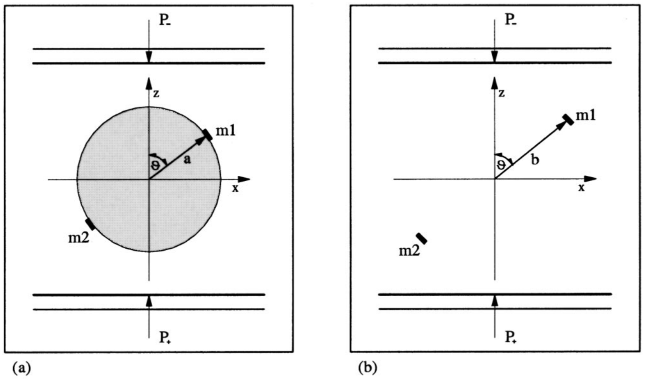

FIG. 1. Plane waves P_+ and P_- incident on (a) a spherical sensor and (b) a two-point sensor.

II. PROBLEM FORMULATION

The geometric configurations of a single-axis spherical sensor and two-point sensor are depicted in Fig. 1. The single-axis spherical sensor consists of two microphones, $m1$ and $m2$, embedded on the surface of a hard sphere with diameter $2a$. The two-point sensor consists of two microphones separated in space by a distance $2b$. The sensors are both centered at the origin. Two plane waves, P_+ and P_-, are incident on the sensors from opposite directions producing a standing wave. The angle of incidence for the wave traveling in the negative z-direction is θ. The complex reflection coefficient of the standing wave is defined by

$$\hat{R}=\frac{\hat{P}_-}{\hat{P}_+}=\eta e^{j\xi}, \tag{1}$$

where $\hat{P}_+$ and $\hat{P}_-$ are the complex amplitudes of the plane waves at the origin when there is no obstacle. (''Hat'' accents above variables and constants indicate complex quantities.) Microphone $m1$ is chosen to have a phase mismatch δ_p, and sensitivity mismatch δ_m, with respect to microphone $m2$ given by

$$\frac{\hat{P}_{m1}}{\hat{P}_{m2}}=\delta_m e^{j\delta_p}, \tag{2}$$

when the microphones are co-located in a pressure field. The variables $\hat{P}_{m1}$ and $\hat{P}_{m2}$ represent the complex pressures at the two microphone locations. The sensitivity mismatch in decibels is

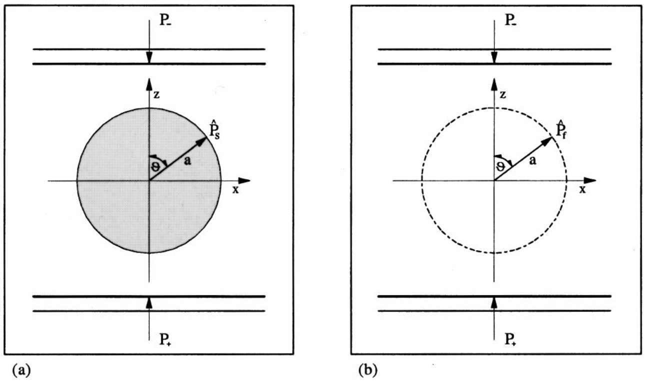

FIG. 2. Plane waves P_+ and P_- incident on (a) a hard-sphere obstacle and (b) no obstacle.

$$\delta_{m,\mathrm{dB}}=20\log\delta_m. \tag{3}$$

Since two microphones are used, only the component along the microphone axis (which will be referred to as the θ-component) of the acoustical measures can be resolved. The θ-components of the potential energy density, kinetic energy density, total energy density, and intensity are defined by

$$U_\theta=\frac{|\hat{P}_c|^2}{12\rho c^2}, \tag{4a}$$

$$T_\theta=\frac{\rho|\hat{V}_\theta|^2}{4}, \tag{4b}$$

$$e_\theta=\frac{|\hat{P}_c|^2}{12\rho c^2}+\frac{\rho|\hat{V}_\theta|^2}{4}, \tag{4c}$$

$$I_\theta=\tfrac{1}{2}\Re e\{\hat{P}_c\hat{V}_\theta^*\}, \tag{4d}$$

where $\hat{P}_c$ is the complex pressure, and $\hat{V}_\theta$ is the complex velocity in the θ-direction at the origin. The phase speed and density of air are given by c and ρ, respectively. The equations including the contributions from all three orthogonal axes for these measures are defined by

$$U_t=\frac{|\hat{P}_c|^2}{4\rho c^2}=U_i+U_j+U_k, \tag{5a}$$

$$T_t=\frac{\rho|\hat{\mathbf{V}}_t|^2}{4}=T_i+T_j+T_k, \tag{5b}$$

$$e_t=\frac{|\hat{P}_c|^2}{4\rho c^2}+\frac{\rho|\hat{\mathbf{V}}_t|^2}{4}=e_i+e_j+e_k, \tag{5c}$$

$$\mathbf{I}_t=\tfrac{1}{2}\Re e\{(\hat{P}_c\hat{V}_i^*,\hat{P}_c\hat{V}_j^*,\hat{P}_c\hat{V}_k^*)\}=(I_i,I_j,I_k), \tag{5d}$$

where

$$\hat{\mathbf{V}}_t=(\hat{V}_i,\hat{V}_j,\hat{V}_k) \tag{6}$$

is the complex particle velocity vector at the origin. The complex conjugate operation is indicated by ''$*$,'' while the real part is indicated by ''$\Re e$.'' The three orthogonal axes are represented by subscripts i, j, and k. Using the finite sum and finite difference approximations, the estimated pressure and velocity at the origin are

$$\hat{P}_{ec}=\frac{\hat{P}_{m2}+\hat{P}_{m1}}{2}, \tag{7}$$

$$\hat{V}_{e\theta}=\frac{\hat{P}_{m2}-\hat{P}_{m1}}{j\rho c2kd}, \tag{8}$$

where d is a constant related to the microphone separation distance.[14]

To determine the bias errors, approximations for the acoustical measures using the finite sum and difference equations are compared to the true values at the origin. The expressions for the four biases are defined by

$$U_{b,\mathrm{dB}}=10\log U_{\mathrm{bias}}=10\log\left|\frac{\hat{P}_{ec}}{\hat{P}_c}\right|^2, \tag{9a}$$

$$T_{b,\mathrm{dB}}=10\log T_{\mathrm{bias}}=10\log\left|\frac{\hat{V}_{e\theta}}{\hat{V}_\theta}\right|^2, \tag{9b}$$

$$e_{b,\mathrm{dB}}=10\log e_{\mathrm{bias}}=10\log\left(\frac{e_{e\theta}}{e_\theta}\right), \tag{9c}$$

$$I_{b,\mathrm{dB}}=10\log I_{\mathrm{bias}}=10\log\left(\frac{I_{e\theta}}{I_\theta}\right). \tag{9d}$$

The true acoustical values at the origin are given by

$$\hat{P}_c=\hat{P}_+(1+\hat{R}), \tag{10a}$$

$$\hat{V}_\theta=\hat{P}_+\frac{(1-\hat{R})\cos\theta}{\rho c}, \tag{10b}$$

$$e_\theta=\frac{|\hat{P}_+|^2}{12\rho c^2}(|1+\hat{R}|^2+3|1-\hat{R}|^2\cos^2\theta), \tag{10c}$$

$$I_\theta=\frac{|\hat{P}_+|^2(1-|\hat{R}|^2)\cos\theta}{2\rho c}. \tag{10d}$$

The normalized complex pressure in the field at point (x,y,z) is given by

$$\hat{P}(z)=(e^{-jkz}+\hat{R}e^{jkz}), \tag{11}$$

for a standing wave. There is no loss in generality of Eqs. (10a)–(10d) by assuming $z=0$ for the standing wave situation since the reflection coefficient, $\hat{R}$, is complex.

III. SCATTERING EFFECTS FROM A HARD SPHERE

The pressure on the surface of the sphere, due to scattering, must be determined to calculate the bias errors of the spherical sensor. The geometry of the problem is depicted in Fig. 2. Two plane waves, P_+ and P_-, form a standing wave with reflection coefficient $\hat{R}$. The hard sphere is centered at the origin. From the equation of scattering of a single plane wave by a sphere,[15] it can be shown that the complex pressure on the surface of a sphere in a standing wave field is given by

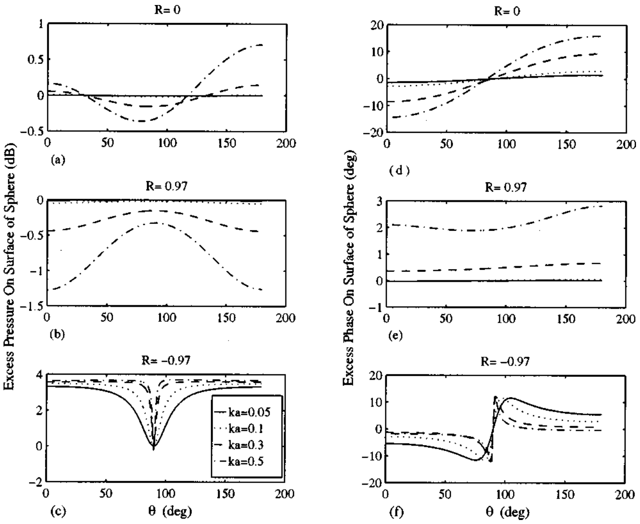

FIG. 3. Excess pressure magnitude and phase on the surface of a hard sphere for various reflection coefficients and values of *ka*.

$$\hat{P}_s(ka,\theta,\hat{R},\hat{P}_+) = \frac{\hat{P}_+}{j(ka)^2}\sum_{n=0}^{\infty}\frac{j^n(2n+1)(\hat{R}+(-1)^n)P_n(\cos\theta)}{h_n^{(2)\prime}(ka)}, \quad (12)$$

where $P_n(\cos\theta)$ is a Legendre function of order *n*, and $h_n^{(2)\prime}$ is the derivative of the spherical Hankel function of the second kind of order *n*. The $e^{j\omega t}$ convention is used here for the complex representation. The pressure on this same surface with the sphere removed, shown in Fig. 2(b), is given by

$$\hat{P}_f(ka,\theta,\hat{R},\hat{P}_+) = \hat{P}_+ e^{-jka\cos\theta} + \hat{P}_+\hat{R}e^{jka\cos\theta}. \quad (13)$$

The complex excess pressure is defined by

$$\hat{P}_{\text{ex}} = \frac{\hat{P}_s}{\hat{P}_f}, \quad (14)$$

and is plotted in Fig. 3 for three values of real reflection coefficient, *R*, and four values of *ka*. To numerically calculate the excess pressure and phase, the first 13 terms in the infinite series of Eq. (12) were used. In Fig. 3(a)–(c), the magnitude of the excess pressures on the surface of a sphere are plotted for $R=0$ (the plane wave case), and $R=\pm 0.97$ (the standing wave cases). Reflection coefficients of ± 0.97 are consistent with the absorption characteristics of an enclosure used by the authors for ANC experiments. When $R=0.97$ the pressure field has a maximum at the sensor location, while when $R=-0.97$ the pressure field has a minimum at the sensor location. Figure 3(d)–(f) show the corresponding phases of the excess pressures on the surface of the sphere. The effects of the sphere are obviously more substantial as ka increases.

For the plane wave case in Fig. 3(a) and (d), there is increased pressure where the plane wave first contacts the sphere at $\theta=180$ deg. The scattering effects on the phase shown in Fig. 3(d) are substantial. The authors have determined that the excess phase varies linearly with ka, indicating a time delay. This time delay yields an effective increase in the acoustic path from one microphone to the other, to be discussed later in this paper. When $R=0.97$ the sensor is at a pressure maximum and a velocity minimum. Here, the sphere has a minimal effect on the pressure field. Both the magnitude and phase of the excess pressure in Fig. 3(b) and (e) are small and relatively uniform. The most significant effect on the magnitude of the excess pressure is seen in Fig. 3(c). In this case, the standing wave field produces a velocity maximum at the location of the sensor. The high velocity of air impinging on the sphere causes a substantial pressure increase, since the pressure without an obstacle present is very small. This also causes the phase to be significantly affected, as seen in Fig. 3(f). Ultimately, the effects of the sphere will cause the bias estimates from finite sum and finite difference for the pressure and velocity estimations to generally improve. This will be seen in plots later in this paper.

The hard sphere effectively changes the acoustic separation of the two microphones embedded on the sphere. The acoustic wave no longer has a direct path from one microphone to the other, but has to travel the contour of the sphere. For a single plane wave propagating in the positive *z*-direction, the reflection coefficient $R=0$, and the pressure on the surface of the sphere becomes

$$\hat{P}_s(ka,\theta,\hat{R}=0,\hat{P}_+) = \frac{\hat{P}_+}{(ka)^2}\sum_{n=0}^{\infty}(-j)^n(2n+1)P_n(\cos\theta) \times\left\{\frac{(ka)^{n+2}}{1\cdot 3\cdot 5\cdots(2n-1)(n+1)}\right\}. \quad (15)$$

The small ka approximation of Eq. (15) is given by[15]

$$\hat{P}_s(ka,\theta,\hat{R}=0,\hat{P}_+) \approx \hat{P}_+(1-j\tfrac{3}{2}ka\cos\theta). \quad (16)$$

Using the finite difference equation Eq. (8) and Eq. (16), the approximate velocity calculated at low frequency for the spherical sensor using $d=a$ would be

$$\hat{V}_{e\theta} \approx \frac{\hat{P}_+ 3ka\cos\theta}{\rho c 2ka}. \quad (17)$$

The constant d is related to the microphone separation distance. (Its exact value will be developed in the next section.) The approximate velocity at low frequency for the two-point sensor under these conditions where $d=b$ is

$$\hat{V}_{e\theta} = \frac{\hat{P}_+ 2\sin(kb\cos\theta)}{\rho c 2kb} \approx \frac{\hat{P}_+ 2kb\cos\theta}{\rho c 2kb}, \quad (18)$$

using Eqs. (8) and (11). The expressions for the velocity calculated for the spherical sensor and the two-point sensor differ only by the factors $3/a$ and $2/b$, respectively. Therefore, the effective separation of the microphones on the sphere is $\frac{3}{2}$ that of the two-point sensor. For subsequent discussion and comparisons, the microphone separation, *b*, of the two-point sensor will be assumed to be $\frac{3}{2}$ the microphone separation, *a*, of the spherical sensor. Thus $ka=\frac{2}{3}kb$.

IV. NUMERICALLY CALCULATED BIAS ERRORS

A. Reflection coefficient and microphone mismatch parameters

The bias error equations become quite complex, especially for the case of the spherical sensor which requires an infinite sum. In order to plot the errors, specific values of the reflection coefficient are chosen. Reflection coefficients of materials are typically not available; however, absorption coefficients are. The absorption coefficient, α, of a material is defined as the energy absorbed by the material divided by the energy incident, which can be written as

$$\alpha=\frac{|\hat{P}_{+}|^{2}-|\hat{P}_{-}|^{2}}{|\hat{P}_{+}|^{2}}. \tag{19}$$

From Eq. (1), $|\hat{P}_{-}|^{2}=|\hat{R}\hat{P}_{+}|^{2}$, and for a purely real reflection coefficient

$$\alpha=1-R^{2}. \tag{20}$$

The walls of the ANC test enclosure consist of sand sandwiched between wood layers, and the absorption coefficient of the walls was estimated to be 0.06. This is equivalent to a reflection coefficient of 0.97. The sensor is located at a pressure maximum if the reflection coefficient is 0.97, while the sensor is located at a pressure minimum if the reflection coefficient is -0.97. The pressure maxima and minima are of interest since the finite sum and difference approximations are particularly subject to error there. A plane wave propagation in the positive z-direction occurs for a reflection coefficient of 0, and is also of interest. Hence, reflection coefficients of ± 0.97 and 0 are used when plotting bias errors.

Specific values of microphone magnitude and phase mismatch are also introduced to plot the bias errors. Measurements of the microphones have shown that they exhibit a first-order roll-off near the 3-dB low-frequency cutoff frequency. The low-frequency cutoff frequency of the microphones varied between 4 and 40 Hz. The microphones also exhibit a second order roll-off near 20 kHz. As an approximation, the response of the microphones was modeled as the first-order high-pass transfer function

$$H(j2\pi f)=\frac{j2\pi f}{j2\pi f+2\pi f_{p}}, \tag{21}$$

near the low-frequency cutoff frequency, f_p, since the high-frequency break frequency is almost two orders of magnitude greater than f_p. From Eq. (21) the phase response, in degrees, would be

$$\angle H(j2\pi f)=90-\frac{180}{\pi}\tan^{-1}\frac{f}{f_{p}}. \tag{22}$$

From Eq. (22), a low-frequency cutoff frequency variation of 4 to 40 Hz between microphones causes a maximum phase variation of approximately 16 deg at 100 Hz between the microphones. This phase variation is much too high for determining acoustic vector quantities with any degree of accuracy. Therefore, the microphone pairs were selected to have less than 1 deg phase mismatch at 100 Hz. Assuming that the microphones would be calibrated with regard to sensitivity by using a simple trim potentiometer, there will still be some sensitivity drift even over short periods of time. It was observed that the microphones varied ±0.25 dB in the laboratory. Hence, phase mismatches of ±1 deg, and sensitivity mismatches of ±0.25 dB, are used for the microphone pairs when plotting bias errors.

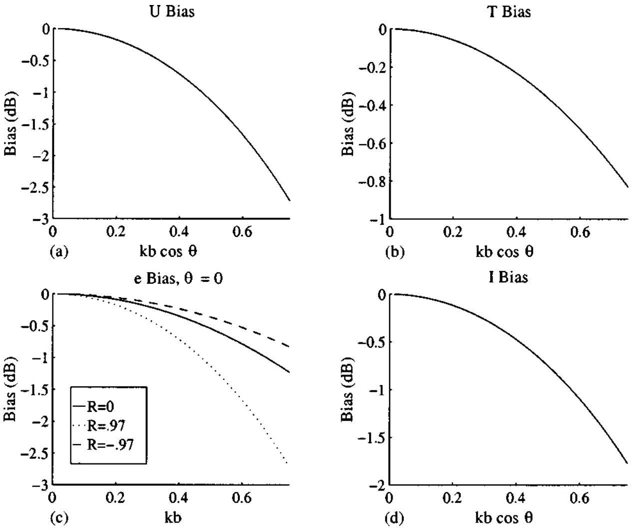

FIG. 4. Bias errors of a two-point sensor with perfectly matched microphones for (a) potential energy density, (b) kinetic energy density, (c) total energy density, and (d) magnitude of intensity measurements.

B. Bias errors of sensors with matched microphones

For the two-point sensor, the bias errors can be calculated using Eqs. (4) and (7)–(10). The normalized complex pressures at the microphones can be found using Eq. (11), where $z=b\cos\theta$ and are given by

$$\hat{P}_{m1}=\delta_{m}e^{j\delta_{p}}(e^{-jkb\cos\theta}+\hat{R}e^{jkb\cos\theta}), \tag{23a}$$

$$\hat{P}_{m2}=(e^{jk\cos\theta}+\hat{R}e^{-jkb\cos\theta}). \tag{23b}$$

For matched microphones, $\delta_m=1$ and $\delta_p=0$. In Fig. 4, the bias errors are plotted for the two-point sensor with matched microphones. The potential and kinetic energy density as well as the intensity bias errors are not a function of the reflection coefficient. The total energy density bias error is dependent on the real reflection coefficient, R, and angle of incidence, θ, and must be plotted for specific values of each. For different reflection coefficients, the relative contributions of the kinetic and potential energy density change in the total energy density measurement. This is also true for different angles of incidence.

In determining the bias errors for the spherical sensor, only the first 13 terms of Eq. (12) are used, since including more terms does not change the results noticeably. The normalized complex pressures at the two microphones in this case are

$$\hat{P}_{m1}=\delta_{m}e^{j\delta_{p}}\frac{\hat{P}_{s}(kd,\theta,\hat{R},\hat{P}_{+})}{\hat{P}_{+}}, \tag{24a}$$

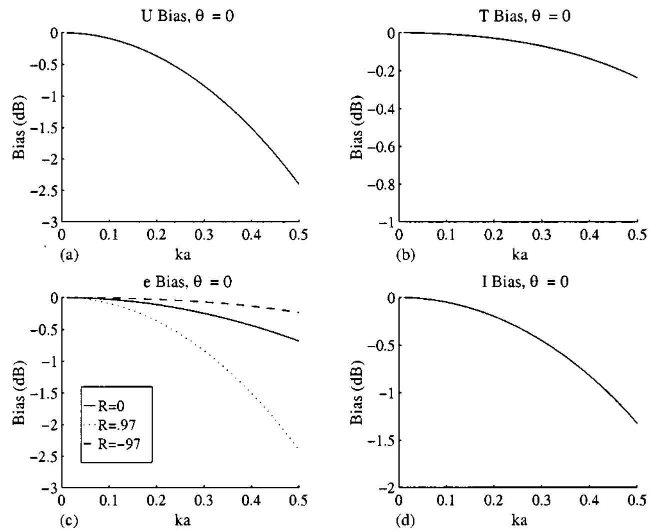

FIG. 5. Bias errors of a spherical sensor with perfectly matched microphones for (a) potential energy density, (b) kinetic energy density, (c) total energy density, and (d) magnitude of intensity measurements.

$$\hat{P}_{m2}=\frac{\hat{P}_s(kd,\theta+\pi,\hat{R},\hat{P}_+)}{\hat{P}_+}, \tag{24b}$$

where $d=\frac{3}{2}a$. Again, the bias errors can be calculated using Eq. (4) and Eqs. (7)–(10). In Fig. 5, the bias errors are plotted for the spherical sensor with matched microphones.

As Elko noted in his work, there is a general improvement in the bias errors due to the diffraction of the hard sphere.[13] The smallest improvement in the total energy density bias occurs when $R=0.97$. Earlier it was seen that the diffraction effects due to the sphere were minimal for this reflection coefficient compared to $R=-0.97$ and $R=0$. The diffraction of the sphere also causes all the bias errors to be a function of ka and θ separately, so that specific angles of θ must be chosen for plotting. The errors of the two-point sensor increase as $\cos\theta$ approaches unity, so the angle chosen for plotting the bias errors was 0, in order to yield the greatest errors.

C. Bias errors of sensors with mismatched microphones

For matched microphones the bias errors are relatively small. If a sensitivity and phase mismatch are allowed in the microphones, a dramatic effect is seen on the bias errors. The spherical sensor and two-point sensor bias errors are plotted in Fig. 6, for the case of 1 deg phase and 0.25-dB sensitivity mismatch in a standing wave field where $R=0.97$, and the angle of incidence is 0.

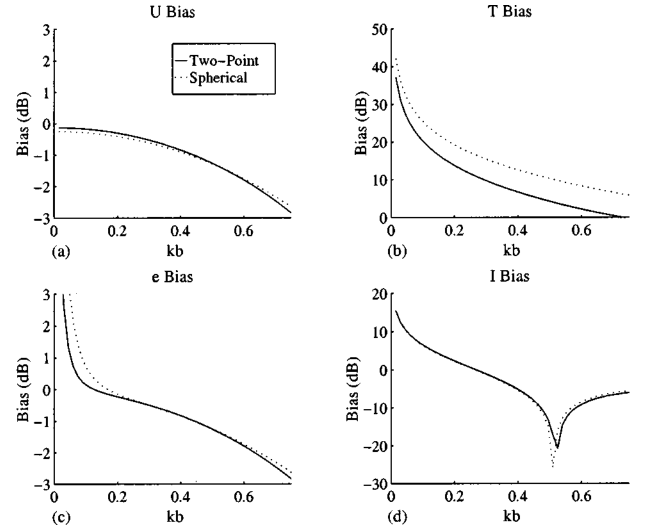

FIG. 6. Bias errors of a spherical sensor and two-point sensor for microphones having a 1-deg phase and 0.25-dB sensitivity mismatch. Sensors are in a standing wave field with reflection coefficient $R=0.97$ and incident angle $\theta=0$. (a) Potential energy density bias, (b) kinetic energy density bias, (c) total energy density bias, (d) magnitude of intensity bias.

As compared to Figs. 4 and 5, the errors in general have significantly increased. There is no longer an improvement in bias errors due to spherical scattering, and generally the errors are dominated by the sensitivity and phase mismatch of the microphones. An important point in comparing the spherical and two-point sensors is that the bias errors show the same trends.

V. TWO-POINT SENSOR BIAS EQUATIONS

The bias error equations for the spherical sensor are intractable due to the infinite series involved. Since the bias error plots for the two-point sensor and the spherical sensor follow the same trends, insight into the bias errors can be gained by studying the bias error equations for the two-point sensor alone. In the case of the two-point sensor, the estimated pressure and velocity using the finite sum and finite difference equations, respectively, are

$$\hat{P}_{ec}=e^{j(\delta p/2)}[(\delta_m+1)(\cos A+\hat{R}\cos B)$$
$$+j(\delta_m-1)(\sin A+\hat{R}\sin B)], \tag{25a}$$

$$\hat{V}_{e\theta}=\frac{je^{j(\delta p/2)}}{\rho c2kd}[(\delta_m-1)(\cos A+\hat{R}\cos B)$$
$$+j(\delta_m+1)(\sin A+\hat{R}\sin B)], \tag{25b}$$

where

$$A=\frac{\delta_p}{2}-kd\cos\theta \quad\text{and}\quad B=\frac{\delta_p}{2}+kd\cos\theta.$$

It follows from Eqs. (7)–(10) that the bias equations are then

$$U_{\mathrm{bias}}=\frac{2\eta(\delta_m^2\cos(\xi+\sigma)+2\delta_m\cos\xi\cos\delta_p+\cos(\xi-\sigma))}{4(1+\eta^2+2\eta\cos\xi)}+\frac{2\delta_m(\cos(\delta_p-\sigma)+\eta^2\cos(\delta_p+\sigma))+(1+\delta_m^2)(1+\eta^2)}{4(1+\eta^2+2\eta\cos\xi)}, \tag{26a}$$

$$T_{\mathrm{bias}}=\frac{2\eta(\delta_m^2\cos(\xi+\sigma)-2\delta_m\cos\xi\cos\delta_p+\cos(\xi-\sigma))}{\sigma^2(1+\eta^2-2\eta\cos\xi)}-\frac{2\delta_m(\cos(\delta_p-\sigma)+\eta^2\cos(\delta_p+\sigma))-(1+\delta_m^2)(1+\eta^2)}{\sigma^2(1+\eta^2-2\eta\cos\xi)}, \tag{26b}$$

$$e_{\mathrm{bias}}=\frac{U_{\mathrm{bias}}|1+\hat{R}|^2+3T_{\mathrm{bias}}|1-\hat{R}|^2\cos^2\theta}{|1+\hat{R}|^2+3|1-\hat{R}|^2\cos^2\theta}, \tag{26c}$$

$$I_{\mathrm{bias}}=\frac{\delta_m(\sin(\delta_p-\sigma)+\eta^2\sin(\delta_p+\sigma)+2\eta\cos\xi\sin\delta_p)}{\sigma(\eta^2-1)}, \tag{26d}$$

where $\sigma=2kd\cos\theta$; ξ and η are defined in Eq. (1). A bias greater than unity indicates an estimate which is high, while a bias between zero and unity indicates an estimate which is low. Negative biases for the velocity or intensity indicate that the vector is 180 deg out of phase. Biases substantially deviating from unity indicate large errors.

The expression for the intensity bias in Eq. (26d) is relatively simple, and clearly indicates the potential for large errors. When the microphones are not phase matched, bias errors increase as σ approaches zero, such as at low frequency and/or an angle of incidence approaching 90 deg. Bias errors also become very large when the numerator of Eq. (26d) approaches zero for finite σ. For $|\sigma|\ll 1$ (in radians) and $|\delta_p|\ll 1$ (in radians), Eq. (26d) can be approximated as

$$I_{\mathrm{bias}}\approx\frac{\delta_m(\sigma(\eta^2-1)+\delta_p|1+\hat{R}|^2)}{\sigma(\eta^2-1)}. \tag{27}$$

The numerator of Eq. (27) becomes zero when

$$\sigma=\frac{\delta_p|1+\hat{R}|^2}{(1-\eta^2)}. \tag{28}$$

Therefore, a finite intensity can yield an intensity estimate of zero, and result in infinite error. The value of σ where this occurs is proportional to δ_p, and therefore the phase mismatch should be kept as small as possible.

The kinetic energy density bias, in Eq. (26b), is a function of $1/\sigma^2$ and the error becomes large for finite phase mismatch as σ approaches zero. For $|\sigma|\ll 1$, the measurement error for the kinetic energy density will be substantially greater than the intensity error, since the intensity bias is a function of $1/\sigma$. The bias errors in kinetic energy density will be greatest when the sensor is at a velocity minimum, when phase mismatches are present in the microphones. The pressures at the two microphones will be large, but very nearly the same in magnitude and phase. Small changes in the microphone phase due to microphone phase mismatch therefore yield a relatively large pressure difference and estimated velocity. At pressure minima, the magnitude of the pressure is low, but the phase gradient is large. Small phase mismatches in the microphones, therefore, have much less of an effect on the estimated velocity in this case.

The expression for the potential energy density in Eq. (26a) is not a function of $1/\sigma$, and therefore does not have the very large errors for small σ as in the intensity and kinetic energy density estimates. For $|\sigma|\ll 1$ rad, and $|\delta_p|\ll 1$, Eq. (26a) can be approximated as

$$U_{\mathrm{bias}}\approx\frac{(1+\delta_m)^2|1+\hat{R}|^2+2\sigma\eta(1-\delta_m^2)\sin\xi+2\sigma\delta_m\delta_p(1-\eta^2)}{4|1+\hat{R}|^2}. \tag{29}$$

When the value of R is not close to -1, the first term in the numerator of Eq. (29) dominates the expression, and Eq. (29) reduces to

$$U_{\mathrm{bias}}\approx\frac{(1+\delta_m)^2}{4}. \tag{30}$$

If $|\delta_{m,\mathrm{dB}}|<1$ dB, then

$$U_{\mathrm{bias}}\approx\sqrt{\delta_m} \tag{31}$$

and

$$U_{b,\mathrm{dB}}\approx\tfrac{1}{2}\delta_{m,\mathrm{dB}}. \tag{32}$$

Hence, the potential energy density bias in decibels for small microphone mismatches and small σ is equal to one-half the sensitivity mismatch in decibels.

The equation for the total energy density bias, Eq. (26c), illustrates that the error is a function of the potential and kinetic energy density bias. The error is high for the kinetic energy density when the sensor is located at a velocity minimum, but the kinetic energy density is quite small compared to the potential energy density. The potential energy density error is relatively small here and dominates the total energy density calculation. Thus the potential energy density mitigates the error due to the kinetic energy density calculation. In general, the errors for the kinetic energy density and potential energy density will not both be high at the same locations, and the errors are reduced for the total energy density calculation.

VI. NUMERICALLY CALCULATED BIAS ERRORS FOR A SPHERICAL SENSOR

A. Results of a single-axis, two-microphone sensor

The bias errors of the spherical sensor were shown to be consistent with the bias errors of the two-point sensor, as illustrated in the previous sections. The spherical sensor also provides a very convenient way of mounting the microphones that is more compact than the two-point sensor by a factor of $\frac{2}{3}$. For these reasons, the spherical sensor is the more attractive sensor and will be studied further in this paper. In this section, the bias errors of the spherical sensor are calcu-

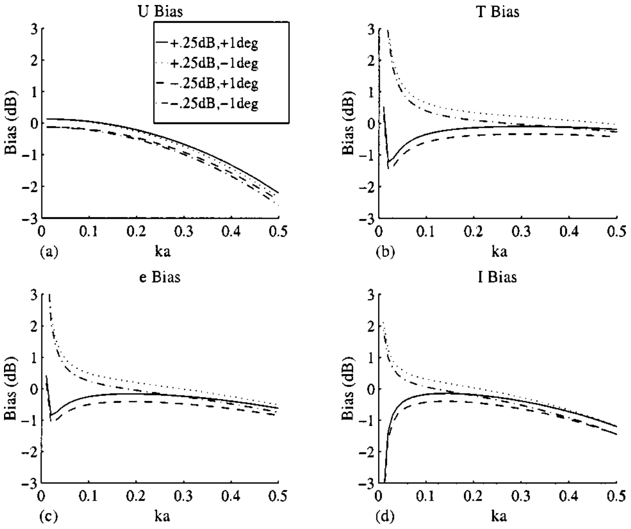

FIG. 7. Bias errors of a spherical sensor with sensitivity and phase mismatched microphones. $R=0$, $\theta=0$. (a) Potential energy density bias, (b) kinetic energy density bias, (c) total energy density bias, (d) magnitude of intensity bias.

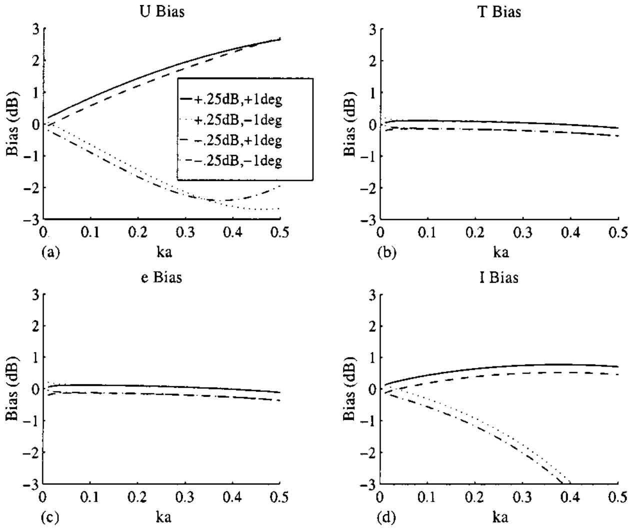

FIG. 9. Bias errors of a spherical sensor with sensitivity and phase mismatched microphones. $R=-0.97$, $\theta=0$. (a) Potential energy density bias, (b) kinetic energy density bias, (c) total energy density bias, (d) magnitude of intensity bias.

lated numerically and plotted for specific parameter values. The bias errors were determined using Eqs. (7)–(10), Eqs. (24), and the first 13 terms of the infinite series in Eq. (12).

The following three figures, Figs. 7–9, show the bias errors for the spherical sensor for reflection coefficients of 0 and ±97. Four plots are overlaid for each subplot for microphones having a sensitivity mismatch of ±0.25 dB, with a phase mismatch of ±1 deg. Figure 7 shows the bias errors for the spherical sensor in a plane wave field, while Figs. 8 and 9 show the bias errors for the spherical sensor in standing wave fields producing a pressure maximum and a pressure minimum at the sensor location, respectively.

The angle of incidence is chosen to be zero for all cases, since this generally yields poor estimations in the total energy density measurement. Earlier, it was shown that the intensity bias error has a singularity for angles of incidence approaching 90 deg. The velocity is zero, but the estimated velocity is finite due to the microphone mismatch. The kinetic energy density and intensity errors are therefore very large. Since the θ-component of the velocity is very small, in this case, the velocity contribution to the total energy density is insignificant. The pressure estimate is very accurate in this case; therefore the total energy density error is low.

The plots for the spherical sensor bias errors are consistent with the analysis conducted on the two-point sensor bias equations in the previous section. In each figure, the potential energy density bias plots show the bias error approaching $\frac{1}{2}\delta_{m,\mathrm{dB}}$ (or ±0.125 dB) for small ka. The kinetic energy density bias error, on the other hand, becomes asymptotically large as ka approaches zero due to its dependence on $1/\sigma^2$. It is difficult to see this in Fig. 9(b) since the error diverges very close the y-axis. The intensity error is similar to the kinetic energy density for very small ka, but the error is not as severe due to its dependence on $1/\sigma$ instead of $1/\sigma^2$. The intensity error also has the singularity indicated by Eq. (28) and seen in Fig. 8(d). The total energy density bias error appears as a combination of the potential and kinetic energy density errors. In all three figures, the potential and kinetic energy densities exhibit larger errors when the sensor is located at a respective minima. When one measurement exhibits large errors, the other does not. The quantity producing the larger error does not contribute to the total energy density as much as the quantity that has smaller errors. Therefore, the total energy density measurement has smaller errors than both. This is true except at low frequencies, where the kinetic energy density approximation swamps out the mitigating effects of the potential energy density approximation. The total energy density bias errors are within ±1 dB for $.03<ka<.3$ for all the plots. This analysis indicates that the total energy density has the smallest bias errors of all four measurements, except for very small values of ka, when finite sum and difference approximations are used.

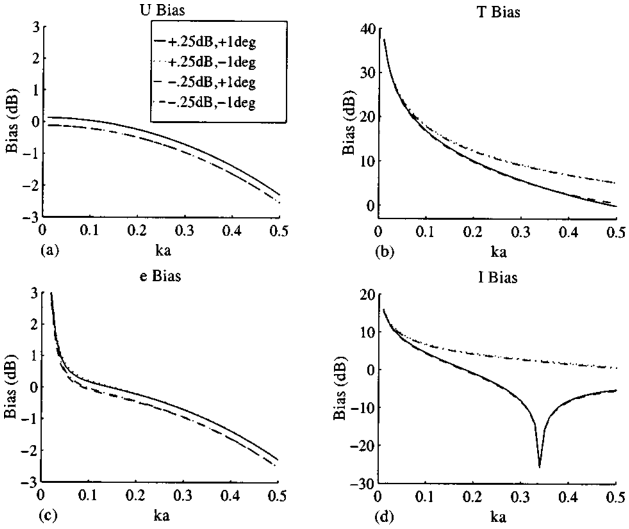

FIG. 8. Bias errors of a spherical sensor with sensitivity and phase mismatched microphones. $R=0.97$, $\theta=0$. (a) Potential energy density bias, (b) kinetic energy density bias, (c) total energy density bias, (d) magnitude of intensity bias.

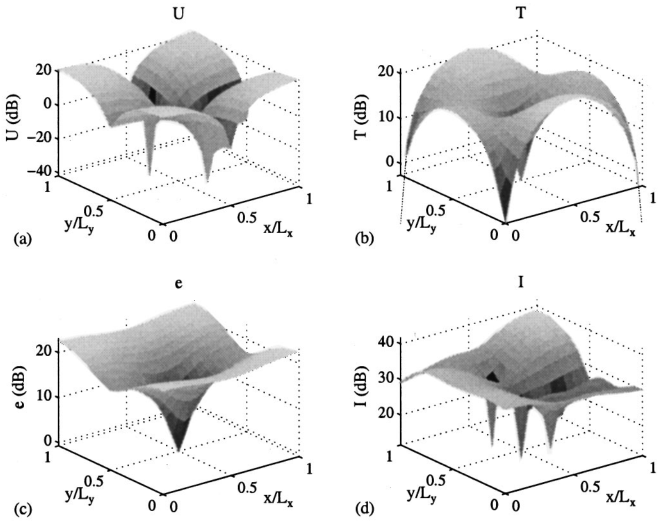

FIG. 10. Predicted (a) potential energy density, (b) kinetic energy density, (c) total energy density, and (d) magnitude of intensity, in the $z/L_z = 0.4$ plane for 135.8 Hz, mode (1, 1, 0) excitation.

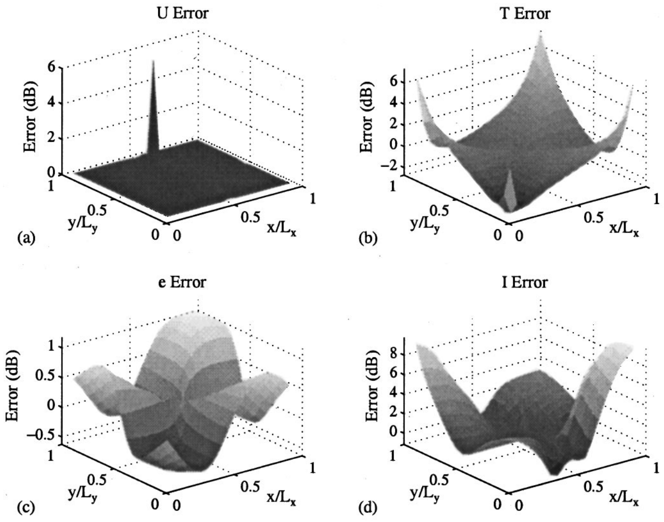

FIG. 11. Predicted spherical sensor error for microphones with a 0.25-dB sensitivity and 1-deg mismatch. (a) Potential energy density bias, (b) kinetic energy density bias, (c) total energy density bias, and (d) magnitude of intensity bias, in the $z/L_z = 0.4$ plane for 135.8 Hz, mode (1, 1, 0) excitation.

B. Results of a three-axes, six-microphone sensor

The bias errors for a three-axis spherical sensor in a three-dimensional pressure field were predicted with a simulation. The sensor employs six microphones oriented along three orthogonal axes. A simulation program generates the pressure and velocity fields within a rectangular enclosure due to a point monopole source. The enclosure's dimensions are 1.5×2.4×1.9 m, having one corner at the origin and the other at (1.5, 2.4, 1.9). The source was located at the normalized point in space (0.12, 0.97, 0.97), where normalized coordinates are defined as $(x/L_x, y/L_y, z/L_z)$. The absorption coefficients used for the walls were $\alpha_x = 0.0479$, $\alpha_y = 0.0313$, and $\alpha_z = 0.0730$. These parameters are consistent with an enclosure used by the authors for ANC experiments. Since the errors in measurements are mostly due to the microphone mismatches, the diffraction effects of the sphere were not modeled. The sphere used in the simulation had a radius of 1 in (0.0254 m), consistent with the size of the sensor ultimately constructed. One microphone from each axis pair was offset in sensitivity by 0.25 dB and 1 deg in phase. Thus each microphone pair had a sensitivity and phase mismatch. The excitation frequency of the enclosure was chosen to be 135.8 Hz, corresponding to the sixth mode, with mode indices (1, 1, 0). An on-resonance frequency was chosen due to the variety of pressure and phase gradients created by on-resonance excitation.

The potential, kinetic, and total energy density, as well as the magnitude of the intensity, were calculated in the $z/L_z = 0.21$ plane; these plots are shown in Fig. 10. The reference value for each of the quantities was chosen to be unity when calculating magnitudes of the fields in units of decibels. The complex pressures were then calculated numerically for each of the six microphones on the sensor. One microphone in each of the axis pairs was offset in sensitivity and phase. The estimated acoustic fields were then determined using Eqs. (4)–(10), where $d = \frac{3}{2}a$. These fields were compared to the actual predicted fields yielding errors as a function of space in the $z/L_z = 0.21$ plane. The error plots are shown in Fig. 11.

It can be seen in Fig. 11 that the smallest errors occur for the total energy density estimation. The error surface is smooth with no singularities or large gradients. The potential energy density estimation has small errors except in one region where it has a sharp peak located at a pressure node. The kinetic energy density estimation has higher errors than the potential energy density estimation, and again the largest errors are at most of the nodes. In this case, the velocity nodes are in the corners and center of the enclosure. As expected, the intensity errors are large since the enclosure is lightly damped. The intensity errors are highest in general where the velocity estimation is poor. As in the two-dimensional sensor analysis, the pressure dominates the total energy density when the velocity error is high, while the velocity dominates the total energy density when the pressure error is high. In the corners of the enclosure, the total energy density estimate improves as the velocity contribution is decreased. The total energy density estimate ensures no singularities in the error. The results of the three-axes spherical sensor are consistent with the analysis for the two-axes sensor. Overall, the magnitudes of the errors in the total energy density estimate are less than 1 dB, which is expected to be low enough for use in an active control system.

VII. EXPERIMENTALLY MEASURED BIAS ERRORS FOR A SPHERICAL SENSOR

The previous analyses indicate the magnitude of the errors associated with a spherical sensor when measuring vector field acoustic quantities. A spherical vector-field sensor was constructed and then tested in a three-dimensional rectangular enclosure consistent with the previous computer simulations. A photograph of two sensors is shown in Fig. 12. A two-inch-diameter wooden ball purchased from a craft store was used as the hard sphere for housing the microphones. Three microphone pairs were mounted along the

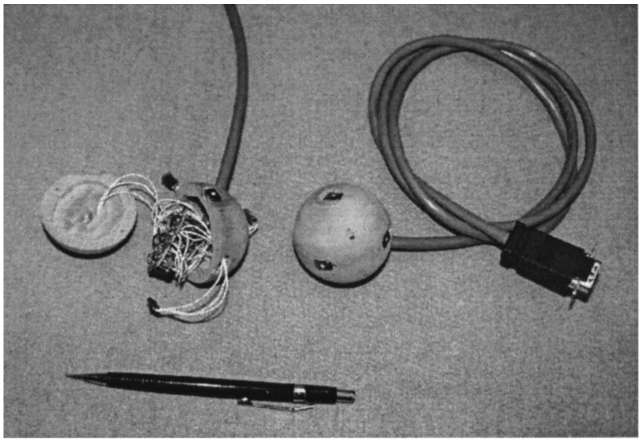

FIG. 12. Two energy density sensors. Sensor diameter is 2 in.

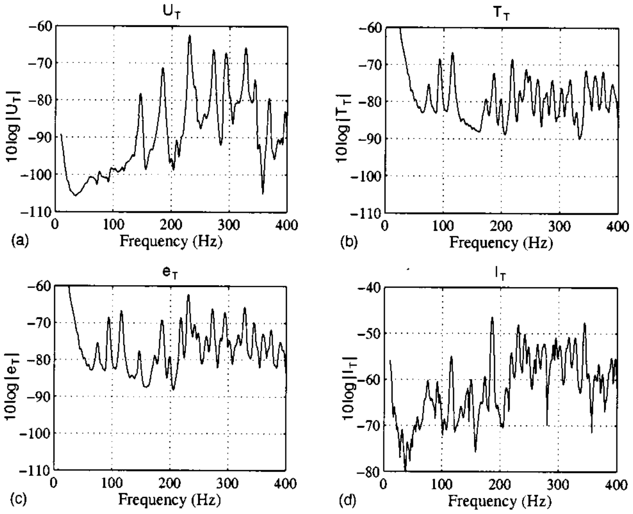

FIG. 13. Two-point sensor experimental measurements. Sensor located at (0.50, 0.50, 0.50). (a) Potential energy density, (b) kinetic energy density, (c) total energy density, (d) intensity.

three orthogonal axes. Each pair was used to estimate the acoustic velocity along its axis as well as the average acoustic pressure. The wooden sphere was cut in two and hollowed to make room for bias and gain circuits, while the surface was routed to allow the microphones to be flush-mounted. A cable with a connector termination provides power and signal connections. The sensor on the left is open, revealing the electronic circuit board inside. The total cost of a sensor was approximately \$100, \$90 of which was for the microphones.

Two sensor locations were chosen for the experiments. One location was in the center of the enclosure at a normalized location of (0.50, 0.50, 0.50), while the other was chosen to be off-center at a normalized location of (0.32, 0.62, 0.64). The sensor was placed in the center of the enclosure due to the many maxima and minima located there, while it was placed off-center to be located in a more random position. Three speakers were placed in close proximity to each other, in a corner of the enclosure to achieve high enough sound pressure levels off-resonance for accurate measurements. A white noise signal was used as the excitation.

A B&K 4135 $\frac{1}{4}$-in diameter matched-microphone pair was used as a two-point sensor to determine the reference measurements. Measurements were taken with the microphone pair aligned with the *x*-, *y*-, and *z*-axes to yield the three orthogonal components of potential, kinetic and total energy density, as well as intensity. A HP 35665A dynamic signal analyzer was used to measure the acoustic quantities along a single axis using the following formulas:

$$U_\theta=\frac{G_1+G_2+2\,\mathrm{Re}\{G_{12}\}}{48\rho c^2}, \tag{33a}$$

$$T_\theta=\frac{G_1+G_2-2\,\mathrm{Re}\{G_{12}\}}{32\rho d^2\omega^2}, \tag{33b}$$

$$e_\theta=U_\theta+T_\theta, \tag{33c}$$

$$I_\theta=\frac{-1}{\rho 4 d\omega}\mathrm{Im}\{G_{12}\}, \tag{33d}$$

where $d=b$, one-half the microphone spacing.[10] The autospectral densities of microphones $m1$ and $m2$ are G_1 and G_2, respectively, while G_{12} is the microphone cross-spectral density. These formulas can be derived from Eqs. (4), (7), and (8) for stationary signals. The three orthogonal components of the acoustic quantities were postprocessed in the software MATLAB™ to yield the complete measurements using Eqs. (5). The acoustic quantities for the spherical sensor were determined the same way, except $d=\frac{3}{2}a$ was used. The two-point sensor microphone spacing was equal to the spacing of the spherical sensor microphones in the experiments, thus $b=a=1\,\mathrm{in.}(0.0254\,\mathrm{m})$.

The acoustic quantities determined using the B&K setup for the sensor located in the center of the enclosure and off-center are plotted in Figs. 13 and 14, respectively. The reference measurements show many fewer peaks in the potential energy density measurement when the sensor is located in the center of the enclosure compared to off-center, since the nodal surfaces of many acoustic modes pass through the center of the enclosure. There are also many velocity minima at the center of the enclosure, and the kinetic energy density

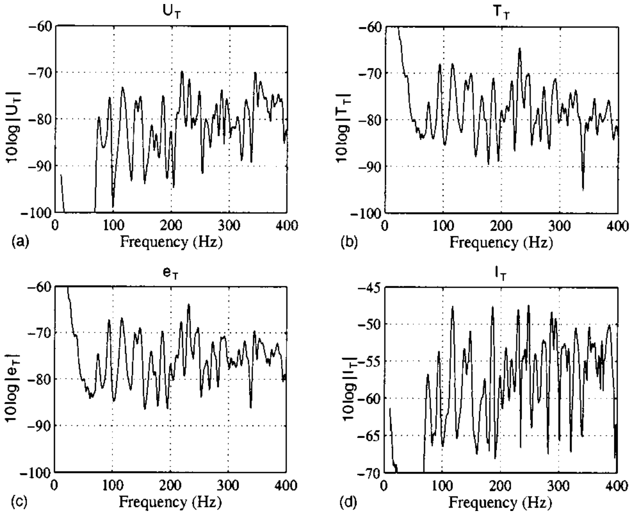

FIG. 14. Two-point sensor experimental measurements. Sensor located at (0.32, 0.62, 0.64). (a) Potential energy density, (b) kinetic energy density, (c) total energy density, (d) intensity.

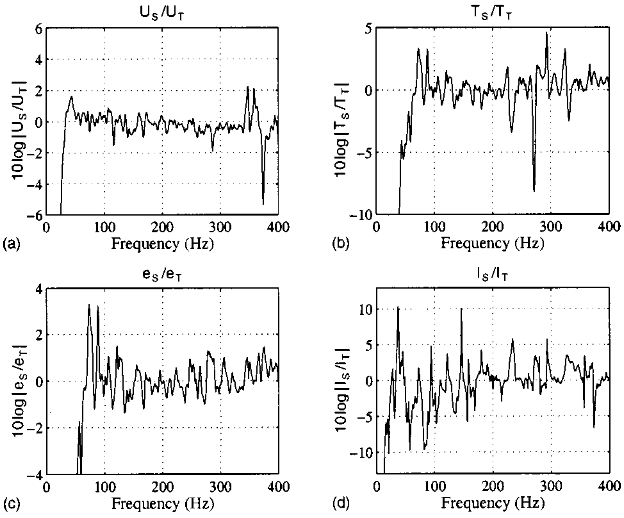

FIG. 15. Difference between two-point sensor measurements and spherical sensor measurements in (a) potential energy density, (b) kinetic energy density, (c) total energy density, and (d) intensity. Sensors located at (0.50, 0.50, 0.50).

measurements show many fewer peaks at that location as well, compared to the off-center location. The total energy density plots have peaks where the potential or kinetic energy density have peaks.

The differences between the spherical sensor measurements and the two-point sensor measurements are shown in Figs. 15 and 16. The differences are due to the sensitivity and phase mismatch of the spherical vector-field sensor, diffraction due to the sphere, and experimental error. The experimental error is mainly due to the inability to remove and replace the sensors so that they are located in exactly the same point in space.

The total energy density estimate using the spherical sensor is within ±1.75 dB of the measurement made using the matched-microphone B&K setup in the frequency region $110<f<400$ Hz. All the other estimates produce errors larger than the total energy density estimate in this frequency region. Under 110 Hz the errors for the total energy density increase due to the $1/\sigma^2$ term in the bias equation. As in the three-dimensional field simulation, the energy density measurement tends to smooth out the largest errors from the potential and kinetic energy density measurements.

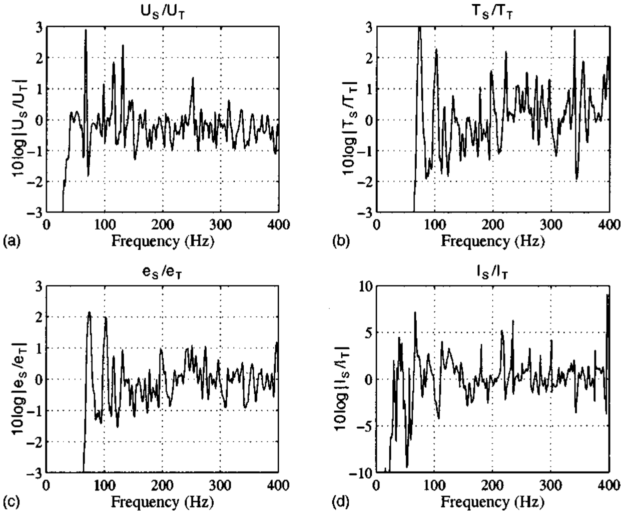

FIG. 16. Difference between two-point sensor measurements and spherical sensor measurements in (a) potential energy density, (b) kinetic energy density, (c) total energy density, and (d) intensity. Sensors located at (0.32, 0.62, 0.64).

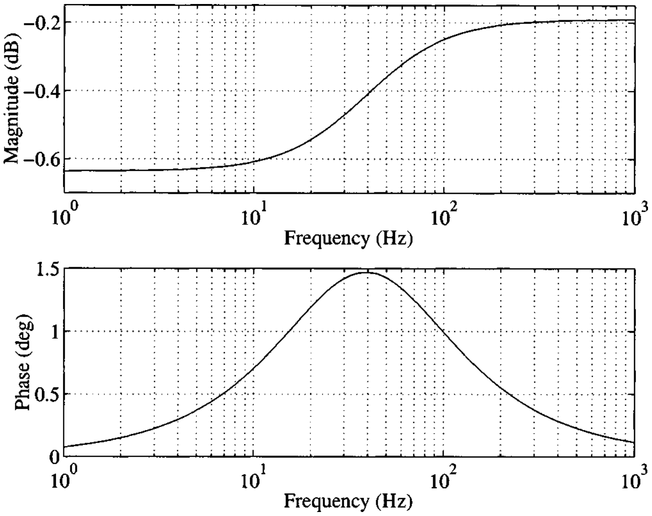

FIG. 17. Bode plot of transfer function between two microphones having a sensitivity mismatch of 0.25 dB and phase mismatch of 1 deg at 100 Hz.

The errors at low frequency can be even higher than those predicted by the previous analysis. From Eq. (21), the transfer function between two microphones having sensitivity and phase mismatch is given by

$$H(j2\pi f)=\delta_m\,\frac{j2\pi f+2\pi f_{p1}}{j2\pi f+2\pi f_{p2}}. \tag{34}$$

A Bode plot of this transfer function is shown in Fig. 17, where the cutoff frequencies are $f_{p1}=38$ and $f_{p2}=40$ Hz. These cutoff frequencies yield a phase mismatch of 1 deg at 100 Hz. The microphones are also given a −0.25-dB sensitivity mismatch.

The previous analysis assumed a constant sensitivity and phase mismatch as a function of frequency, however Fig. 17 shows this not to be true. The phase error increases as the frequency is reduced below 100 until 40 Hz, but decreases as the frequency is increased above 100 Hz. The sensitivity mismatch can also increase at low frequency, depending on the microphone phase/sensitivity combination. Thus the errors in total energy density can be higher than those expected at frequencies lower than the cutoff frequency, but may improve at higher frequencies. The cutoff frequency for the microphones used is no higher than 40 Hz. So long as the energy density sensor is used to measure fields with frequency content above 40 Hz, the acoustical estimates should be more nearly accurate than those predicted by the simulations.

VIII. SUMMARY

Two configurations of a vector-field sensor were studied in this paper with regard to measurement error. The estimates of potential, kinetic, and total energy density as well as intensity were investigated. The spherical sensor's errors are similar in magnitude to the two-point sensor's, yet had two beneficial features. The spherical sensor provides a convenient way of mounting and locating the sensor microphones, and the diffraction effects of a spherical sensor cause an increase in the effective separation of the microphones. Thus a spherical sensor can be made smaller by a factor of $\frac{2}{3}$ while maintaining the same accuracy as a two-point sensor.

It was shown that the spherical sensor generally improves the accuracy of the acoustical measurements when the sensor microphones are matched in sensitivity and phase. When the microphones are mismatched, however, the effects of the microphone mismatch dominate the errors, and there is no longer a significant improvement in accuracy due to diffraction effects around the sphere. It was also shown that a vector-field sensor could be constructed with inexpensive electret microphones, where the accuracy of the total energy density error could be kept within ±1.75 dB for two measurements in the $110 < f < 400$-Hz frequency range. The errors seen in the experimental measurements showed the same trends as those predicted by theory and simulation.

ACKNOWLEDGMENTS

The authors would like to thank the Applied Research Laboratory at Penn State University and NASA Langley for funding this research.

[1] A. E. Schwenk, S. D. Sommerfeldt, and S. I. Hayek, ''Adaptive control of structural intensity associated with bending waves in a beam,'' J. Acoust. Soc. Am. **96**, 2826–2835 (1991).

[2] S. D. Sommerfeldt and B. L. Scott, ''Wavenumber sensors for active control of acoustic radiation,'' in *Proceedings of the 1993 North American Conference on Smart Structures and Materials*, 1993, Vol. 1917, pp. 612–622.

[3] X. Pan, T. J. Sutton, and S. J. Elliott, ''Active control of sound transmission through a double-leaf partition by volume velocity cancellation,'' J. Acoust. Soc. Am. **105**, 2828–2835 (1998).

[4] S. J. Elliot, P. A. Nelson, I. M. Stothers, and C. C. Boucher, ''In-flight experiments on the active control of propeller-induced cabin noise,'' J. Sound Vib. **140**, 219–238 (1990).

[5] S. D. Sommerfeldt and P. J. Nashif, ''Energy based control of the sound field in enclosures,'' *Second International Congress on Recent Developments in Air and Structure-Borne Sound and Vibration*, March, 1992, pp. 361–368.

[6] P. J. Nashif, ''An energy-density-based control strategy for minimizing the sound field in enclosures,'' M.S. thesis, Pennsylvania State University, University Park, PA, 1992.

[7] S. D. Sommerfeldt and J. W. Parkins, ''An evaluation of active noise attenuation in rectangular enclosures,'' *Proc. Inter-Noise 94*, pp. 1351–1356 (1994).

[8] S. D. Sommerfeldt, J. W. Parkins, and Y. C. Park, ''Global active noise control in rectangular enclosures,'' *Proc. ACTIVE 95*, pp. 477–488 (1995).

[9] J. W. Parkins, S. D. Sommerfeldt, and J. Tichy, ''Narrowband and broadband active control in an enclosure using the acoustic energy density,'' J. Acoust. Soc. Am. **108**, 192–203 (2000).

[10] F. J. Fahy, *Sound Intensity* (E. & F.N. Spon, London, 1995), pp. 91–97.

[11] I. Wolff and F. Massa, ''Use of pressure gradient microphones for acoustical measurements,'' J. Acoust. Soc. Am. **4**, 217–234 (1933).

[12] R. K. Cook and P. A. Schade, ''New method for measurement of the total energy density of sound waves,'' *Proc. Inter-Noise 74*, pp. 101–106 (Oct. 1974).

[13] G. W. Elko, ''An acoustic vector-field probe with calculable obstacle bias,'' *Proc. Noise-Con 91*, pp. 525–532 (July 1991).

[14] F. J. Fahy, ''Measurement of the acoustic intensity using the cross-spectra-density of two microphone sensors,'' J. Acoust. Soc. Am. **62**, 1057–1059 (1977).

[15] P. M. Morse and K. U. Ingard, *Theoretical Acoustics* (Princeton University Press Reprint 1986, McGraw-Hill, New York, 1968), pp. 418–421.